ELSEVIER

Measurement of the cosmic ray composition at the knee with the SPASE-2/AMANDA-B10 detectors

AMANDA and SPASE Collaborations

J. Ahrens [a], M. Ackermann [b], E. Andres [c], X. Bai [d,1], S.W. Barwick [e,*], R.C. Bay [f], T. Becka [a], K.-H. Becker [g], E. Bernardini [b], D. Bertrand [h], F. Binon [h], A. Biron [b], D.J. Boersma [b], S. Böser [b], O. Botner [i], A. Bouchta [i], O. Bouhali [h], T. Burgess [j], S. Carius [k], T. Castermans [l], D. Chirkin [f], J. Conrad [i], J. Cooley [c], D.F. Cowen [m], A. Davour [i], C. De Clercq [p], T. DeYoung [c,2], P. Desiati [c], J.-P. Dewulf [h], E. Dickinson [n,1], P. Ekström [j], R. Engel [d,3], P. Evenson [d,1], T. Feser [a], T.K. Gaisser [d,1], R. Ganugapati [c], M. Gaug [b], H. Geenen [g], L. Gerhardt [e], A. Goldschmidt [o], A. Hallgren [i], F. Halzen [c], K. Hanson [c], R. Hardtke [c], T. Hauschildt [b], M. Hellwig [a], P. Herquet [l], G.C. Hill [c], J.A. Hinton [n,1], D. Hubert [p], B. Hughey [c], P.O. Hulth [j], K. Hultqvist [j], S. Hundertmark [j], J. Jacobsen [o], A. Karle [c], J. Kim [e], L. Köpke [a], M. Kowalski [b], K. Kuehn [e], J.I. Lamoureux [o], H. Leich [b], M. Leuthold [b], P. Lindahl [k], I. Liubarsky [q], J. Lloyd-Evans [n,1], J. Madsen [r], K. Mandli [c], P. Marciniewski [i], H.S. Matis [o], C.P. McParland [o], T. Messarius [g], T.C. Miller [d,4], Y. Minaeva [j], P. Miočinović [f,5], P.C. Mock [e,6], R. Morse [c], R. Nahnhauer [g], T. Neunhöffer [a], P. Niessen [p], D.R. Nygren [o], H. Ögelman [c], Ph. Olbrechts [p], C. Pérez de los Heros [j], A.C. Pohl [j], R. Porrata [e,7], P.B. Price [f], G.T. Przybylski [o], K. Rawlins [c], E. Resconi [b], W. Rhode [g], M. Ribordy [b], S. Richter [c], K. Rochester [n,1], J. Rodríguez Martino [j], D. Ross [e], H.-G. Sander [a], T. Schmidt [b], K. Schinarakis [g], S. Schlenstedt [b], D. Schneider [c], R. Schwarz [c], A. Silvestri [e], M. Solarz [f], G.M. Spiczak [r,1], C. Spiering [b], M. Stamatikos [c], T. Stanev [d,1],

* Corresponding author. Fax: +1-949-824-2174.

E-mail address: sbarwick@uci.edu (S.W. Barwick).

[1] SPASE Collaboration.

[2] Department of Physics, University of Maryland, College Park, MD 20742.

[3] Present address: Forschungszentrum Karlsruhe, Institut fur Kernphysik, Postfach 3640, 76021 Karlsruhe, Germany.

[4] Present address: Applied Physics Laboratory, Johns Hopkins University, Laurel, MD 20723, USA.

[5] Department of Physics and Astronomy, University of Hawaii, Honolulu, HI 96822, USA.

[6] Present address: SEA Inc. 7545 Metropolitan Dr. San Diego, CA 92108, USA.

[7] Present address: L-174, Lawrence Livermore National Laboratory, 7000 East Ave., Livermore, CA 94550, USA.

D. Steele [c], P. Steffen [b], R.G. Stokstad [o], K.-H. Sulanke [b], I. Taboada [s],
S. Tilav [d,1], C. Walck [j], W. Wagner [g], Y.-R. Wang [c], A.A. Watson [n,1],
C.H. Wiebusch [g], C. Wiedemann [j], R. Wischnewski [b], H. Wissing [b],
K. Woschnagg [f], W. Wu [e], G. Yodh [e], S. Young [e]

[a] *Institute of Physics, University of Mainz, Staudinger Weg 7, D-55099 Mainz, Germany*
[b] *DESY-Zeuthen, D-15735 Zeuthen, Germany*
[c] *Department of Physics, University of Wisconsin, Madison, WI 53706, USA*
[d] *Bartol Research Institute, University of Delaware, Newark, DE 19716, USA*
[e] *Department of Physics and Astronomy, University of California, Irvine, CA 92697, USA*
[f] *Department of Physics, University of California, Berkeley, CA 94720, USA*
[g] *Fachbereich 8 Physik, BUGH Wuppertal, D-42097 Wuppertal, Germany*
[h] *Université Libre de Bruxelles, Science Faculty CP230, Boulevard du Triomphe, B-1050 Brussels, Belgium*
[i] *Division of High Energy Physics, Uppsala University, S-75121 Uppsala, Sweden*
[j] *Department of Physics, Stockholm University, SCFAB, SE-10691 Stockholm, Sweden*
[k] *Department of Technology, Kalmar University, S-39182 Kalmar, Sweden*
[l] *Université de Mons-Hainaut, 19 Avenue Maistriau 7000, Mons, Belgium*
[m] *Department of Physics, Pennsylvania State University, University Park, PA 16802, USA*
[n] *School of Physics and Astronomy, University of Leeds, Leeds LS2 9JT, UK*
[o] *Lawrence Berkeley National Laboratory, Berkeley, CA 94720, USA*
[p] *Vrije Universiteit Brussel, Dienst ELEM, B-1050 Brussel, Belgium*
[q] *Imperial College, London SW7 2AZ, UK*
[r] *Department of Physics, University of Wisconsin, River Falls, WI 54022, USA*
[s] *Departamento de Física, Universidad Simon Bolívar, Apdo. Postal 89000, Caracas, Venezuela*

Abstract

The mass composition of high-energy cosmic rays at energies above 10^{15} eV can provide crucial information for the understanding of their origin. Air showers were measured simultaneously with the SPASE-2 air shower array and the AMANDA-B10 Cherenkov telescope at the South Pole. This combination has the advantage to sample almost all high-energy shower muons and is thus a new approach to the determination of the cosmic ray composition. The change in the cosmic ray mass composition was measured versus existing data from direct measurements at low energies. Our data show an increase of the mean log atomic mass $\langle \ln A \rangle$ by about 0.8 between 500 TeV and 5 PeV. This trend of an increasing mass through the "knee" region is robust against a variety of systematic effects.

1. Introduction

Cosmic rays observed at Earth follow a steep power-law spectrum over many orders of magnitude in energy. At an energy of approximately 3 PeV, however, the spectral index steepens; this feature is called the "knee". To understand the reason for the knee, one must understand the source, acceleration mechanism, and propagation of cosmic rays. For instance, first-order Fermi acceleration, thought to explain cosmic rays below the knee, has a natural cutoff energy which depends on the rigidity of the nucleus being accelerated. Observing the mass composition of cosmic rays at the knee therefore provides an important clue to the origin of cosmic rays.

The study of high-energy cosmic rays has led to the construction of large ground-based air shower

arrays to explore the energy range above 100 TeV where the cosmic ray flux is too low for direct measurements. These arrays, unlike satellite- or balloon-borne instruments, must reconstruct the properties of primary cosmic rays indirectly, from the behavior of the extensive air shower particles produced in the atmosphere. The different particle components of an air shower (electrons, photons, muons, and hadrons) can be measured using different detection techniques. Since the behavior of any one particle component generally depends on both primary energy and primary mass, multi-component measurements are proving to be a powerful detection tool.

One such multicomponent experiment is SPASE/AMANDA, a scintillator array and deep-ice Cherenkov telescope working in coincidence at the South Pole. SPASE measures the electron component of the air showers at the surface, while AMANDA measures muon bundles at depths of 1500–2000 m. By combining electron and muon information, the primary cosmic ray energy and mass can be estimated for each coincidence event.

2. The SPASE and AMANDA detectors

The South Pole Air Shower Experiment (SPASE-2, or SPASE in this paper) is a scintillator array consisting of 120 modules grouped into 30 stations on a 30 m triangular grid. The SPASE site on the surface lies about 400 m from the center of the AMANDA hole locations, at an atmospheric depth of $\sim$685g cm^{-2} [1].

The Antarctic Muon And Neutrino Detector Array (AMANDA) uses the natural ice at the South Pole as the target and detection volume for a large-scale Cherenkov telescope [2]. Currently, an array of 677 optical modules (OM's) containing photomultipliers is frozen in the ice. This work uses data from 1998, in which the detector comprised 302 OM's on 10 strings between depths of 1500 and 2000 m. The OM's measure the Cherenkov light emitted by charged particles traveling faster than the speed of light in ice. AMANDA's primary mission is the detection of high-energy neutrinos by collecting Cherenkov light emitted by their interaction product, a lepton such as a muon.

A neutrino-induced muon is only identifiable by its upgoing direction. Misreconstructed downgoing cosmic ray muons (produced in the atmosphere above the South Pole) constitute the dominant background for neutrino-induced muons, and so great care is taken to remove them from neutrino analyses. In this work, however, cosmic ray muons are the *signal*, rather than the background. Some difficulties of the neutrino analysis can be avoided here, while a cosmic ray analysis presents new and different challenges of its own.

3. Shower reconstruction in SPASE

SPASE data analysis reconstructs the shower direction from the arrival times of charged particles in the array's scintillators. The shower core location and shower size are reconstructed by fitting the lateral distribution of particle density to the Nishimura–Kamata–Greisen (NKG) function [3] and then evaluating this lateral distribution at a fixed distance from the shower core. In particular, SPASE data analysis computes for each event the shower parameter $S(30)$, the measured particle density at 30 m from the shower core, in units of equivalent minimum ionizing vertical muons per m^2. The shower core can be reconstructed within a few meters, and the shower direction to within 1.5° at low energies, improving to less than 0.4° at higher energies [4]. $S(30)$ can be used as an energy estimator, but it is not entirely composition-independent. The shower size depends also on the height of interaction in the atmosphere, which in turn depends on the primary mass. A detailed description of how $S(30)$ is measured can be found in references [1,5].

4. Reconstruction in AMANDA

Just as SPASE is used to reconstruct the position, direction, and electron size of an air shower event, a similar procedure is developed for the analysis of the muon bundle in AMANDA. First, the combined detectors are used to get the bundle's position and direction more accurately than can be achieved using either detector alone. Then, the

expected lateral distribution function (LDF) of photons from a muon bundle is computed. Two corrections must be applied to the LDF in order to be able to apply it to all OM's and all depths. The first accounts for the ranging-out of muons between the top of the detector and the bottom. The second accounts for the changing scattering length in the ice, due to variation of concentration of impurities such as dust in ice. For each event, the LDF is fitted to OM amplitudes and evaluated at a fixed distance of 50 m from the center of the bundle to compute a parameter called $K(50)$. This parameter is analogous to $S(30)$ but measures muon energy loss rather than electron density. The technique is described in more detail below.

4.1. Track reconstruction

The standard AMANDA track reconstruction, described in [6], is performed by the reconstruction program recoos. To reconstruct muon direction in normal operation, recoos varies the position (x, y, z) of a point on the track and its direction (θ, ϕ), until the track hypothesis (a single muon line source) is most likely to have given rise to the observed light pattern. SPASE coincidences, however, provide additional information: the shower core location at the surface (within 3–4 m) and shower direction (within 1.5°). A better track can be found by fixing the track position at the reconstructed shower core in SPASE, using SPASE's reconstructed track as a first guess, and allowing recoos to vary *only* the direction angles (θ, ϕ) as free parameters. The long lever arm between the two detectors (about 1750 m center-to-center) gives this technique great accuracy, less than a half degree. Fig. 1 shows the relative positions of SPASE and AMANDA, and how the SPASE reconstruction alone can be improved by using both detectors with this combined technique.
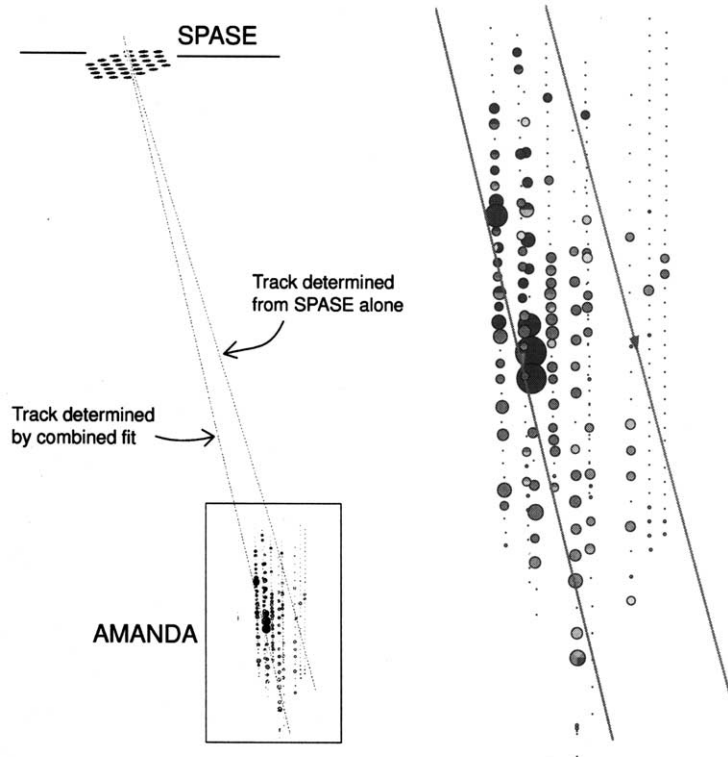

Fig. 1. SPASE/AMANDA coincidence event from 1997 data.

4.2. Muons in AMANDA

High-energy muons (meaning in this context, muons of energy above 300 GeV which can reach the detector at depth) are created by the decay of high-energy charged pions and kaons originating high in the atmosphere in the early stages of shower development. The Gran Sasso laboratories (housing the underground LVD and MACRO experiments) have explored the potential of coincidences between surface electrons from EAS-TOP and TeV muons [7–10]. Due to their small size, MACRO and similar experiments sample only a few individual muons from the air shower. AMANDA is shallower (resulting in a lower muon energy threshold) and also much larger. It can also detect light up to 150 m from the muon bundle. AMANDA can measure the energy loss of the muon bundle at depth, but it is too sparse an array to resolve individual muons. This makes AMANDA a fundamentally different kind of cosmic ray detector, requiring new techniques. Therefore in this paper we must devote some time to the physics of muon bundles emitting light in ice, and the introduction of a new technique for reconstructing the total muon energy loss using photomultiplier pulse amplitudes recorded by AMANDA.

The differential energy spectrum of the muons in a shower at the surface follows a power law with spectral index −2.757 [11]. As the muons penetrate the ice, their energy loss can be described by [12]

$$-\frac{dE_\mu}{dx} = a_{eff} + b_{eff}E_\mu \tag{1}$$

with values of a_{eff} and b_{eff} for ice also taken from [12]. From the surface spectrum and this differential equation, one can calculate the distribution of the number of muons surviving to slant depth X

$$N_{\mu_{depth}}(X) = N_{\mu_{surface}}(> E) = KE^{-1.757}$$

$$= K\left[\left(\frac{a_{eff}}{b_{eff}}\right)(e^{b_{eff}X} - 1)\right]^{-1.757} \tag{2}$$

This equation also describes how the muon intensity within a single event changes as the bundle propagates through the detector from 1500 m at the top to 2000 m at the bottom, illustrated in Fig. 2(a). Simulations of muons propagating through these depths of ice are compared in Fig. 2(b) to this simple functional form, which will be used later for computing the range-out correction to the photon LDF.

Only muons with a surface energy of more than ∼300 GeV survive to AMANDA depth. The transverse momentum of these muons is small
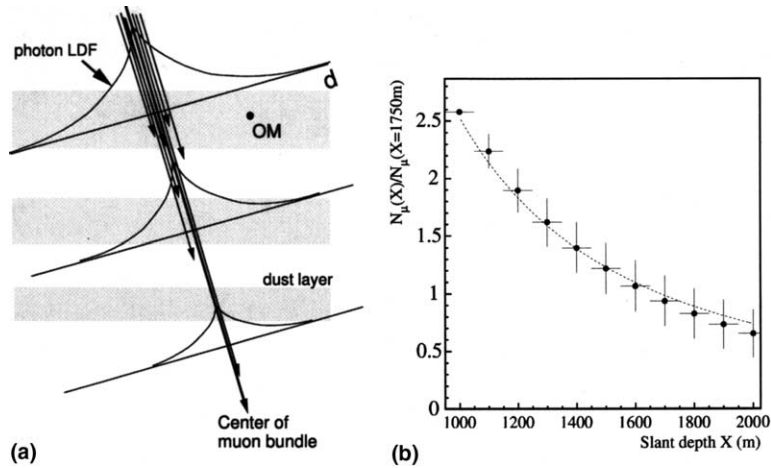

Fig. 2. Propagation of muons through the ice: (a) schematic representation of how the ranging out of muons affects the photon LDF; (b) ratio of muons reaching slant depth X, as a function of X, averaged over many simulated events. The fraction is defined to be relative to the arbitrary reference slant depth of 1750 m, which is the distance from the center of SPASE to the center of AMANDA. Dashed line: Muon fraction calculated using Eq. (2) in the text.

compared to their longitudinal momentum, so the muons are tightly contained in a bundle. Simulations show that on average 90% of all muons reaching the detector level are contained within a radius of $\sim$20 m in 1 PeV proton-induced showers. In iron-induced showers of the same energy this radius increases to $\sim$30 m.

4.3. Light from muons in ice

At the wavelengths relevant to AMANDA, between 300 and 600 nm, impurities (dust) are the most important contributor to both absorption and scattering of light in deep Antarctic ice. A YAG laser at a wavelength of 532 nm was first used to map the effective scattering length, λ_e, and the absorption length, λ_a, as functions of depth [13], revealing vertical fluctuations due to dusty layers of ice. More recently, *in-situ* light emitters at a variety of other wavelengths (470 nm with blue LEDs, 370 nm with UV LEDs, and 337 nm with a Nitrogen laser) [14] have confirmed the predicted wavelength dependence of both scattering [15] and absorption [16].

For a *line* source of light, the photon intensity seen by an OM is the integrated contribution from many infinitesimal length elements. At distances d large compared to λ_e the photon intensity is described by a modified Bessel function of the second kind [16]:

$$I(d) \propto \frac{1}{\lambda_e} K_0(d/\lambda), \tag{3}$$

where d is the perpendicular distance from the OM to the primary track, and λ is an effective propagation length due to the combined effects of absorption and scattering, given by

$$\lambda = \sqrt{\lambda_e \lambda_a / 3} \propto \lambda_e \tag{4}$$

For large enough values of its argument z, the Bessel function K_0, can be approximated as $\sqrt{2/(\pi z)}e^{-z}$. The photon LDF for a particular ice layer can then be described by:

$$I(d) \propto \frac{1}{\lambda\sqrt{d/\lambda}}e^{-d/\lambda} = \frac{1}{\sqrt{d/\lambda}}e^{-d/\lambda} \tag{5}$$

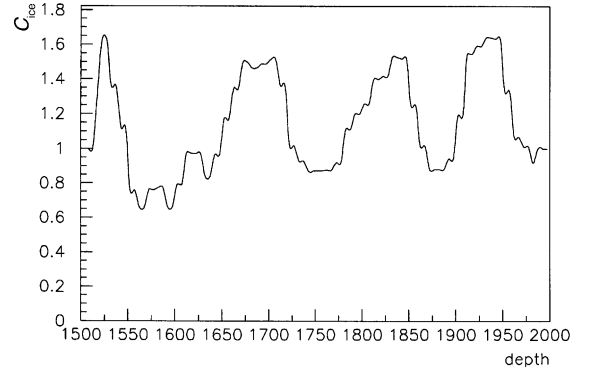At large distances, photons have been travelling through ice layers of different quality, which to-

Fig. 3. The ice correction C_{ice} as a function of depth, from in-ice scattering data.

gether can be described by a bulk ice propagation length $\lambda = \lambda_0$. At near distances, the propagation length of the OM's local ice layer $\lambda = \lambda(z) = c_{\text{ice}}(z)\lambda_0$ is more appropriate. The depth-dependent correction factor $c_{\text{ice}}(z)$, shown in Fig. 3, is taken from in-ice measurements of the variation of scattering length around the average value [13]. For an approximate treatment of the effect of dust layers at *all* distances, the photon LDF can be described by a split function which employs $\lambda(z)$ below a transition distance D and λ_0 above it

$$I(z,d) \propto \begin{cases} \dfrac{1}{\sqrt{\lambda_0 c_{\text{ice}}(z)d}}e^{-d/(\lambda_0 c_{\text{ice}}(z))}, & d < D \\[3mm] \dfrac{1}{\sqrt{\lambda_0 d}}e^{-d/\lambda_0}, & d > D \end{cases} \tag{6}$$

This functional form fits well to data when a value of 80 m, which is comparable to the spacing between depths with peak concentration of dust, is used for the transition distance D.

4.4. Complete LDF fit

The complete photon LDF for all depths and distances incorporates both the range-out correction and the ice correction. An expected OM amplitude $\mathscr{A}$, follows the same functional form and is proportional to the LDF intensity

$$\mathscr{A} = NN_{\mu_{\text{depth}}}(X)I(z,d) \tag{7}$$

where the overall normalization, N, absorbs other normalization factors and also converts the result

into units of OM amplitude (photoelectrons). N is also proportional to the total amount of light emitted by the muon bundle.

With the track position and direction held fixed, recoos maximizes the likelihood $\mathscr{L}$ of the amplitudes measured by AMANDA modules to derive from the expected functional form:

$$\mathscr{L} = \prod_{\text{all OM's}} \mathscr{L}_{\text{OM}} = \prod_{\text{all OM's}} P(\mathscr{A}_{\text{measured}} \,|\, \mathscr{A}), \qquad (8)$$

where P is a Poisson probability. The overall normalization N and the bulk propagation length λ_0 are left as free parameters. N is proportional to the total energy loss of muons in the ice. λ_0 is known from in-ice measurements to be about 26 m [13]. However, errors in track reconstruction can cause a change in the best-fit slope of the LDF. If instead we fit λ_0 as a free parameter and then evaluate the resulting reconstructed LDF at a fixed distance, we can achieve a very stable measurement of the overall muon energy loss. The reconstructed λ_0 can also be used as a cut parameter to ensure that the LDF for the fitted event has been reconstructed sensibly.

The fit LDF is evaluated at a constant distance, in this case 50 m; this distance offers the most stable measurement under simultaneous variations in fitted N and λ_0 due to errors in track reconstruction. The parameter $K50$ is defined as the value of the fit LDF function, evaluated in the absence of correction factors (meaning

$N_{\mu_{\text{depth}}}(X) = 1$ and $c_{\text{ice}}(z) = 1$), and at a distance of 50 m from the primary track

$$K50 = \frac{N}{\sqrt{(50\text{ m})\lambda_0}} e^{-(50\text{ m})/\lambda_0}. \qquad (9)$$

$K50$ is analogous to similar parameters used by other experiments, and is a measurement of muon energy loss. This parameter is also well-correlated with the number of muons in the bundle, shown in Fig. 4(a), and with the total muon energy at the surface, shown in Fig. 4(b) (see Section 5.2 for a description of the simulation procedure). These correlations are nearly composition-independent. $K50$ is not, however, a direct measurement of the number of muons that reach the detector, since it also accounts for the emission and propagation of the Cherenkov light through the ice that surrounds the AMANDA optical modules.

Fig. 5 shows the resolutions of the two parameters we will use together to measure cosmic ray energy and mass: $S(30)$ and $K50$. A measurement of $S(30)$ in SPASE relates to the total number of electrons in the shower, with a resolution shown in Fig. 5 (a): 0.04 in $\log_{10}(N_e)$ for $S(30)$ between 50 and 55 m^{-2}. A measurement of $K50$ in AMANDA relates to the total muon energy, with a resolution shown in Fig. 5(b) 0.10 in $\log_{10}(E_{\mu\,\text{at surface}})$ for $K50$ between 0.9 and 1.1 photoelectron/OM. It may be noted that an event of this brightness generates a total of about 300 photoelectrons summed over all OM's.
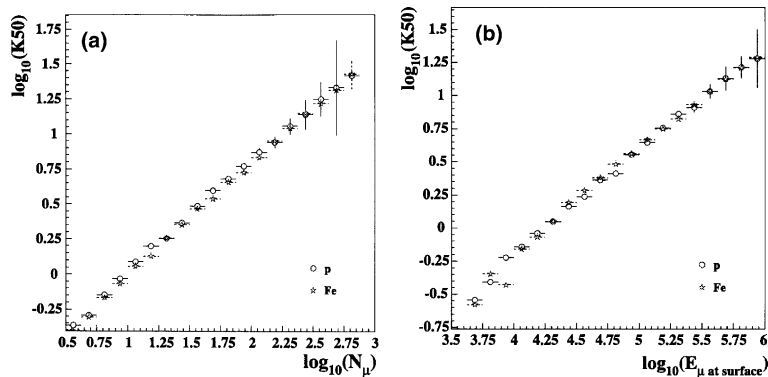

Fig. 4. The reconstructed $K50$ resolution, for proton and iron simulations (the irregularity at low energies is a small-statistics fluctuation): (a) $K50$ vs. the true number of muons at 1750 m slant depth and (b) $K50$ vs. the true total muon energy at the surface.
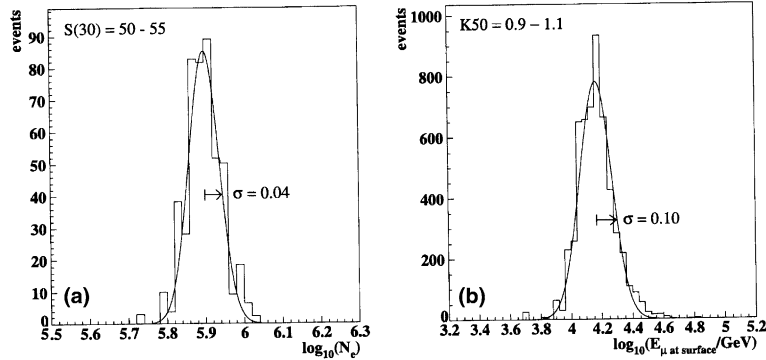
Fig. 5. Resolutions of $S(30)$ reconstructed by SPASE, and $K50$ reconstructed by AMANDA (simulated p,He,O,and Fe nuclei all included): (a) shower size resolution: The distribution of true total number of electrons is shown for events with $S(30)$ in the range 50–55 m^{-2} and (b) muon energy resolution: the distribution of true total muon energy at the surface is given for a $K50$ in the range 0.9–1.1 photoelectron/OM.

5. Data and Monte Carlo samples

5.1. Data

SPASE/AMANDA coincidence data from 1998 were used for the results in this work (though data from 1997 were used first to explore the techniques). AMANDA operated in slave mode to SPASE, reading out all OM's upon receiving an SPASE trigger externally. Events were matched together offline by comparing GPS times (each detector has its own independent clock) and requiring a match within 1 ms. A more detailed description of how SPASE and AMANDA operate in coincidence can be found in [17]. Coincidence events between SPASE and AMANDA have zenith angles of between 8° and 18°, with additional quality cuts confining this range even further.

5.2. Monte Carlo simulations

The simulation used in this work employs a modified version of the air shower code MOCCA [18] using the QGSJET98 interaction model [19]. We simulated 350 000 proton- and iron-induced showers according to an E^{-1} spectrum from energies of 100 TeV to about 100 PeV, and from angles of 0° to 30°. The events are re-weighted to a cosmic ray energy spectrum, with a spectral index of −2.7 below a knee at 3 PeV and −3.0 above it. The

surface component is processed through the SPASE detector simulation. Whenever SPASE is triggered by the simulated air shower, the SPASE scintillator data together with the muon information are recorded. The high-energy muons are then propagated through the ice with the muon propagator PROPMU [20]. The Cherenkov photons generated by the muon are finally propagated through the ice and events are simulated with a detailed AMANDA detector simulation. The systematic uncertainties associated with these simulations will be discussed further on, together with the results.

5.3. Quality cuts

A small set of quality cuts ensures an event sample where both SPASE and AMANDA have reliably reconstructed the track direction and the parameters $S(30)$ and $K50$.

- *The shower is large enough to reconstruct size.* Small showers are not well reconstructed, so an iterative determination of $S(30)$ is not performed when the first determination gave $S(30) < 4$ m^{-2}. All events with $S(30)$ less than m^{-2} are discarded in this analysis at an early stage.
- *The track passes within the AMANDA array.* SPASE tracks which pass *outside* AMANDA tend to get pulled *in* by the combined track fit described in Section 4.1. Thus, we require the

SPASE track of an event to intersect a cylinder of ice representing AMANDA's geometrical volume.

- *The shower core lies within the SPASE array*. The shower core reconstruction and therefore the entire event reconstruction is not reliable if the core is located outside the array. The cut removes about 10% of the data.

- *For small S(30) showers, the track must pass closer to the center of AMANDA*. Angular resolution begins to suffer for small $S(30)$ when fewer AMANDA modules are hit. However, tracks which pass close to the center of AMANDA can still be reconstructed well. Between $S(30) = 5$ and 20 m^{-2}, the cut on track direction is tightened linearly from 1.0 to 0.7 times the geometrical size of AMANDA, in order to preserve good angular resolution without losing too many events.

- *The LDF fit slope is within a reasonable range*. As discussed earlier, the reconstructed effective propagation length λ_0 should resemble what has been independently measured for antarctic ice, but can take on a range of values and still provide a robust $K50$. This slope is required to be between zero and 100. This cut does not have a large impact on the event statistics; it merely removes unphysical outliers.

In 1998 SPASE recorded 28.9 million showers. AMANDA's ontime during that year was 70% of SPASE's. Out of the coincidentally recorded events 16% were pointing at AMANDA and passed the $S(30) > 5m^{-2}$ cut. 70,000 of those events were succesfully reconstructed, and 5655 events survive the additional quality cuts to the final analysis level. From the Monte Carlo sample, 5515 events survive to this level.

6. Measuring cosmic ray energy and composition

When the two observables $K50$ and $S(30)$ are plotted against each other, as in Fig. 6, showers of different primary energy and primary mass can be separated in the two-dimensional parameter space. The higher the primary energy of the event, the more electrons in SPASE and the more muons in
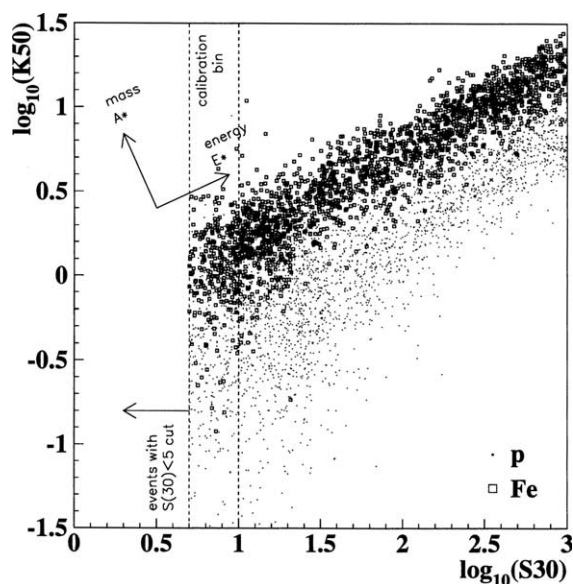

Fig. 6. $S(30)$ vs. JFC50 for simulated proton and iron events. The "calibration bin" of $S(30)$ between 5 and 10 m^{-2}, as well as the directions of the A^* and E^* axes are indicated on the plot.

AMANDA. But for a *given* primary energy, iron-induced showers are more muon-rich than proton-induced showers and $K50$ is enhanced relative to $S(30)$. This can be explained in a simplified way by the superposition principle; a shower from a nucleus of mass A can be approximated as A superimposed proton-like showers, each with $1/A$ of the total primary energy. The larger the A, the smaller the energy fraction carried by each nucleon, and the lower the energies of secondary pions, which are more likely to decay into muons before interacting. Thus, heavy primaries produce more muons for the same primary energy than light primaries.

We can create a set of transformed axes, named E^* and A^*, also shown in Fig. 6. These axes are rotated from $K50$ and $S(30)$ by an angle (determined by simulations) of 24°. Every event can now be identified with coordinates in $E^* - A^*$ space, and these coordinates are used as energy and mass estimators for that event.

Two more steps are necessary to get to a determination of $\langle \ln A \rangle$ itself. First, the absolute scale of $K50$ (the more vulnerable of the two observables to systematic uncertainties) must be calibrated. This is done by calibrating the mass

composition at low energies where direct measurements are available. Second, the data and Monte Carlo simulations are then compared along the E^* and A^* axes to get the best fit mass composition in a series of energy bins.

The analysis presented here uses a 2-component Monte Carlo model (proton and iron primaries). The data are expected to lie somewhere in between, and the mean log mass $\langle \ln A \rangle$ from a mixture of protons and iron is used to characterize the mass composition. A 4-component model (p, He, O, and Fe) was also explored, and is used here as a consistency check.

6.1. Calibrating with direct measurements at low energy

To measure the absolute scale of $K50$ from simulations alone suffers systematic uncertainties from a variety of sources, for instance, the absolute number of muons predicted by the hadronic interaction model or the muon propagation simulation. These uncertainties affect the absolute calibration of the $K50$ parameter, but not the shape or properties of its distribution. Cosmic ray composition is known at low energies from direct measurements up to several hundred TeV; if we calibrate the measurement at low energies to agree with the known composition, we can then investigate whether the composition *changes* as energy increases.

The technique is calibrated at low energies using events with $S(30) = 5$–10 m^{-2}, the vertical "slice" shown in Fig. 6, which corresponds to 200–350 TeV protons and about twice this energy for iron. Monte Carlo events, which are generated over a wide energy range using the same spectral index for each component, are weighted by a relative proportion which represents a mixed composition, or $\langle \ln A \rangle$. This mean log mass at low energy can be taken from direct measurements such as JACEE [21] and RUNJOB [22]. Figure 19 of Ref. [22] shows $\langle \ln A \rangle$ of 2.1 ± 0.2 measured by JACEE between 10^5 and 10^6 GeV and $\langle \ln A \rangle = 1.7 \pm 0.3$ measured by RUNJOB. We have taken a calibration value $\langle \ln A \rangle = 2$.

The distributions of $\log_{10}(K50)$ for data and the calibration mixture of simulated proton and iron within this slice, shown in Fig. 7, agree well in
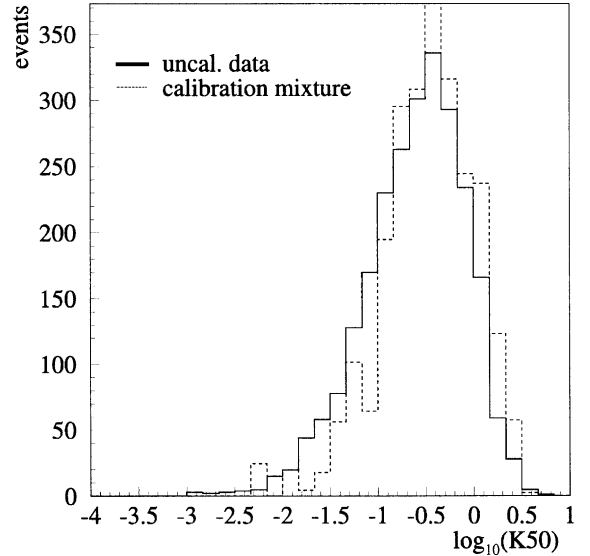

Fig. 7. The distribution of $\log_{10}(K50)$ for uncalibrated data and the calibration mixture.

shape, but not in mean. Hypothesizing that data and Monte Carlo differ by a constant offset ϵ in $\log_{10}(K50)$, we can find the value of ϵ which makes the two histograms agree best using a Kolmogorov–Smirnov test. This renormalization factor is applied to the $\log_{10}(K50)$ of the data for the remainder of this paper. For the baseline model, ϵ is found to be 0.14. Alternative values of ϵ were also analyzed in order to investigate systematic errors; these will be discussed later.

Fig. 8 shows both calibrated and uncalibrated data in the $K50 - S(30)$ parameter space, together with the simulated proton and iron events. Uncalibrated, the data appear unphysically light given our knowledge of mass composition at low energies. Calibrated, the data reveal the trend in mass composition. The seven slanted straight lines drawn represent the constant energies of $\log_{10}(E_{\mathrm{prim}}/\mathrm{GeV}) = 5.6, 5.8, 6.0, 6.2, 6.4, 6.6,$ and 6.8. They form six *bins* of constant energy. A formal procedure for measuring energy and mass is described below.

6.2. Energy resolution

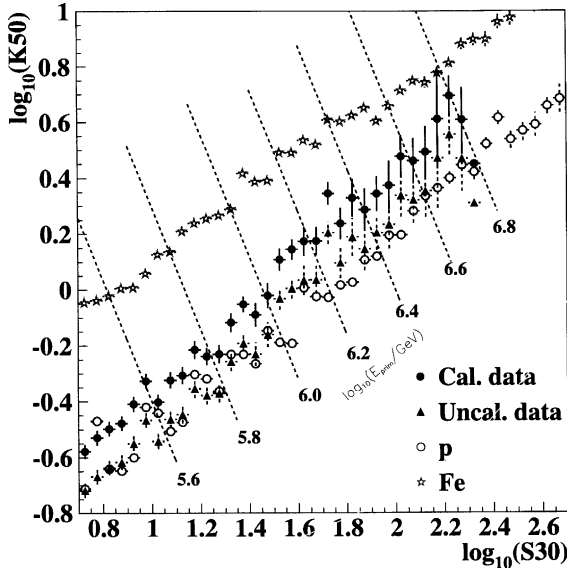The E^* axis is roughly linear in the log of the true primary energy. Using simulations, we

Fig. 8. Uncalibrated and calibrated data, in the $K50 - S(30)$ parameter space, compared to simulated proton and iron events. Constant-energy contours are also shown.
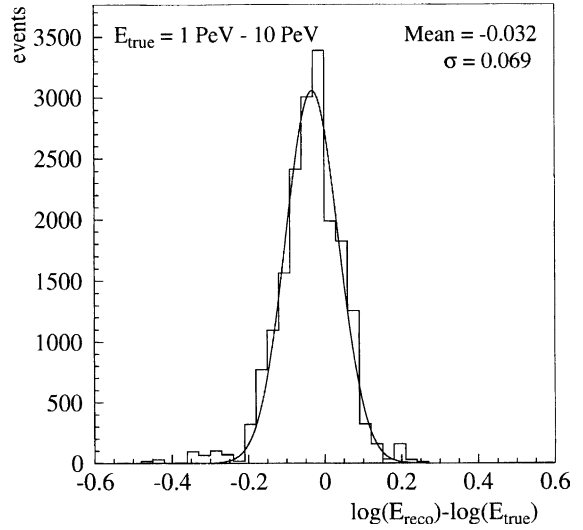

Fig. 9. Distributions of the differences between reconstructed and true energy of an equal mixture of p- and Fe-showers for the energy range from 1 to 10 PeV. The width of the distribution measures the energy resolution. The results are based on full shower and detector Monte Carlo simulations.

compare this energy estimator with the true primary energy $\log_{10}(E_{\mathrm{prim}})$. The relationship is composition-independent, and can be fit by

$$\log_{10}(E_{\mathrm{prim}}/\mathrm{GeV}) = 4.9 + 0.72 \times E^* \qquad (10)$$

The resolution of this line fit is given in Table 1 for five different energy ranges with equal mixtures of proton- and iron-induced showers: $\sigma = 0.12$ in $\log_{10}(E_{\mathrm{prim}})$ at energies near 100 TeV, and improving 0.057 at the highest simulated energies of 30 PeV. The combined detector's response is linear up to about 10 PeV. Fig. 9 shows the energy resolution of proton- and iron-induced air showers

Table 1
Energy resolution of an equal mixture of p- and Fe-induced showers as a function of energy based on full detector simulation of both detectors

$\log_{10}(E/\mathrm{GeV})$	$\log_{10}(E_{\mathrm{reco}}/E_{\mathrm{true}})$	
	μ	σ
5.0–5.5	0.010	0.119
5.5–6.0	−0.041	0.113
6.0–6.5	−0.035	0.072
6.5–7.0	−0.014	0.059
7.0–7.5	−0.026	0.057

in the energy range from 1 to 10 PeV. The average energy resolution is $\sigma = 0.07$ in $\log_{10}(E_{\mathrm{prim}})$.

6.3. Mass resolution

Just as E^* can be used to estimate primary energy, A^* can be used to estimate primary mass for each shower. In particular, to measure cosmic ray composition from the data, we compare the A^* distributions of the data and the Monte Carlo. The proton and iron Monte Carlo events can be mixed with an iron fraction f_{Fe} to reproduce a given $\langle \ln A \rangle$. The mixture which best describes the data is found by scanning through hypothesis mixtures, such as those shown in Fig. 10. The likelihood $\mathscr{L}$ of each hypothesis f_{Fe} is the product over histogram bins of the Poisson probability of observing the number of data events given the number of simulated events in that bin. The most likely f_{Fe} is found at the peak of the resulting likelihood curve, where $\mathscr{L}(f_{\mathrm{Fe}}) = \mathscr{L}_{\max}$. The error on the measurement can be derived from the width of the likelihood curve; if $\mathscr{L}$ is Gaussian in f_{Fe}, then 1σ is the value of f_{Fe} at which [23]
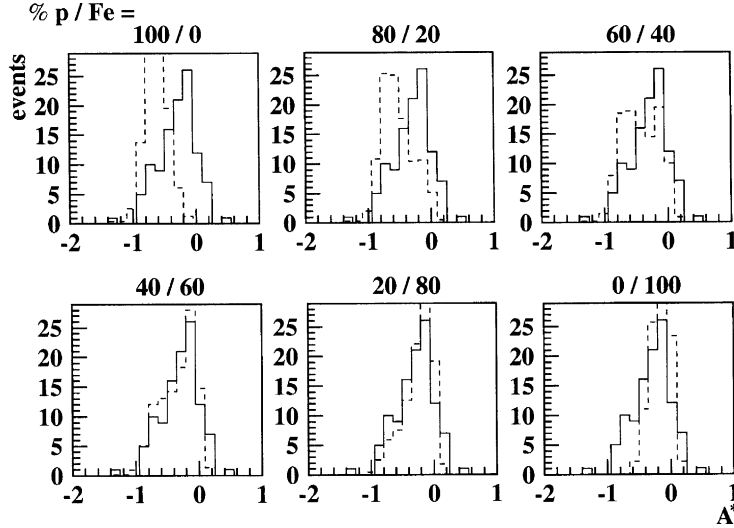
Fig. 10. Sample composition mixtures of p- and Fe-induced showers (dashed), and how they can be compared to data (solid). The double peak structure in the some mixtures illustrates the separation potential between p and Fe.

$$\ln \mathscr{L}(f_{\text{Fe}}) = \ln \left[\mathscr{L}_{\text{max}} \exp \left(-\frac{(1\sigma)^2}{2\sigma^2} \right) \right]$$

$$= \ln \mathscr{L}_{\text{max}} - 1/2 \qquad (11)$$

The simulated histograms are normalized to the data, so the test compares the histogram shapes. The Kolmogorov–Smirnov test was also applied to the histograms as a cross-check, with duplicate results. The procedure was repeated for each of the six energy bins; the results for all six bins are shown in Fig. 11.

6.4. Systematic uncertainties

We are faced with a choice of different shower generation, muon propagation, and detector models, each with a different absolute normalization. However, calibrating data to Monte Carlo in a low-energy calibration bin is a technique adaptable to any model. By treating each model as an independent test of normalization and composition, we can gauge the stability of this technique under changing models, and estimate the systematic error on the final measurement. In addition to a baseline model, several alternatives can serve to test the robustness of the analysis to a variation of parameters. The six models used here are

- *Baseline*. MOCCA/QGSJET, muon propagator PROPMU, 17-layer ice, 2-component (p and Fe) composition.
- *Bulk*. Same as baseline, but with uniform ice. Here we use a simplified ice model which contains no vertical structure.
- *Four component*. p, He, O and Fe nuclei, split into light and heavy groups with equal weight within each group.
- *SIBYLL*. The SIBYLL-17 code [24] is used for the interaction model instead of QGSJET.
- *Amplitude gate*. Here, an incorrect amplitude readout was used in simulating AMANDA electronics, resulting in a loss of photon counting accuracy. Using this model tests the sensitivity of the Monte Carlo to a perturbation in the electronic response.
- *MMC*. The muon propagator PROPMU has been replaced with the propagator MMC [25].

For each model, a calibration constant ϵ was computed, and an independent analysis performed in the same fashion as described above. The same experimental data were compared to each model in the variable A^*, and the mean log mass and error bars for the model were computed from the likelihood curve. The numerical results from the six models are summarized in Table 2. While there are
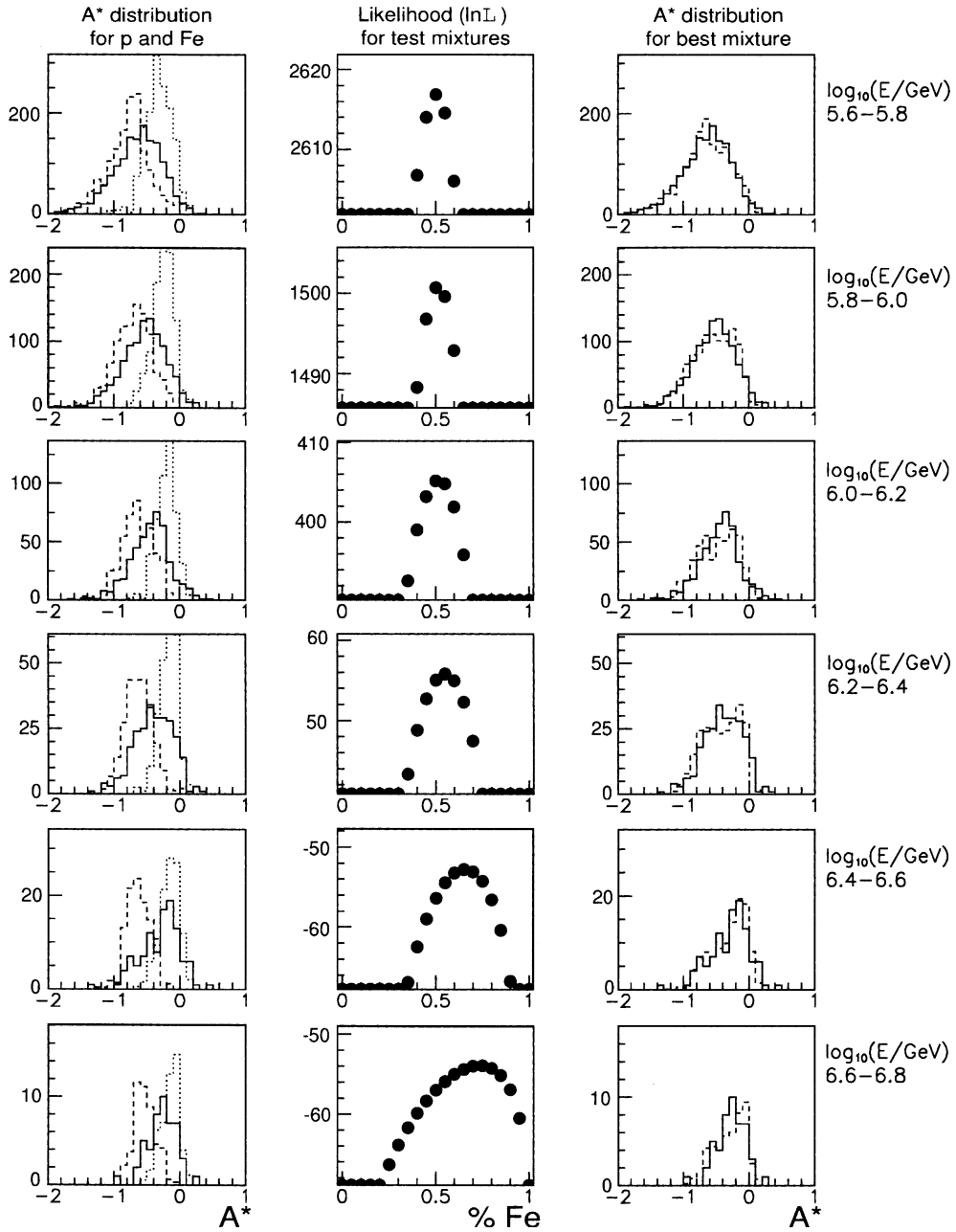
Fig. 11. For the six constant-energy bins: (left) distributions of A^* for pure protons (dashed), pure iron (dotted) and calibrated data (solid); (middle) $\ln(\mathscr{L})$ as a function of iron percentage and (right) distributions of A^* for best mixture of protons and iron (dashed) and calibrated data (solid). Monte Carlo distributions are normalized to data.

systematic shifts in the *absolute* $\langle \ln A \rangle$ between different models, all of the composition measurements follow a similar *trend*.

An additional source of systematic error is uncertainty in the direct measurement at low energy, against which the $K50$ parameter is

Table 2
Summary of composition results from different simulation models

Model	Baseline	Bulk	4 Comp.	SIBYLL	Ampl. gate	MMC
ϵ	0.14	0.06	0.10	0.01	0.14	0.16
$\log_{10}(E/\text{GeV})$	$\langle \ln A \rangle \pm 1\sigma\ (2\sigma)$	$\langle \ln A \rangle$				
5.6–5.8	$1.98 \pm 0.06\ (0.13)$	2.09	1.86	2.08	1.99	2.21
5.8–6.0	$2.00 \pm 0.07\ (0.14)$	2.05	1.91	1.86	2.00	2.15
6.0–6.2	$2.03 \pm 0.10\ (0.21)$	2.22	2.42	1.92	2.03	2.36
6.2–6.4	$2.13 \pm 0.13\ (0.26)$	2.11	2.61	2.13	2.15	2.24
6.4–6.6	$2.62 \pm 0.22\ (0.45)$	2.53	2.61	*	2.56	2.67
6.6–6.8	$2.83 \pm 0.39\ (0.78)$	2.87	3.40	*	2.83	3.2

The asterisk indicates omission due to lack of simulated statistics.

calibrated and the factor ϵ computed. To study this, a variety of different values of ϵ from 0.04 to 0.18 (corresponding to direct measurement $\langle \ln A \rangle$ values between 1.8 and 2.2) were tested. The results are included in the summary, as a distinct source of error.

7. Results and discussion

Fig. 12 shows the mean log mass as a function of the primary energy. Data points indicate the results from the baseline model, normalized to $\langle \ln A \rangle = 2.0$ in the normalization bin, with one standard deviation statistical error bars computed from the likelihood curve. The shaded band indicates the range of results obtained using different simulations, an estimate of the systematic error from models. Note that these error bars are highly asymmetric and the baseline model gives values close to the lower limit. The additional lines indicate results using different initial calibration mixtures, corresponding to ϵ values from 0.04 to 0.18, with the baseline simulation, an estimate of the systematic error from our incomplete knowledge of $\langle \ln A \rangle$ at low energies.

The data show a mass composition consistent with flat between 500 TeV and 1.2 PeV, after which it starts to become heavier. $\langle \ln A \rangle$ increases by 0.9 between 1.2 and 6 PeV. The statistical and systematic errors in the last bins are too large to allow a good determination of growth of $\langle \ln A \rangle$. The data are not consistent, however, with mass becoming lighter through the knee.
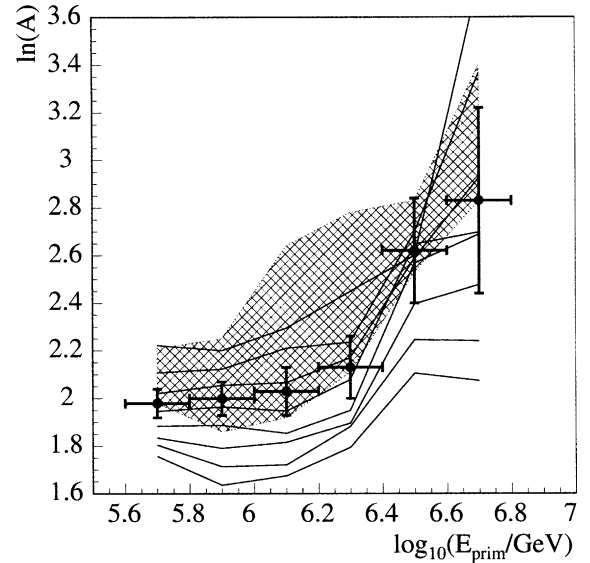

Fig. 12. Change of the mass composition relative to the baseline model as a function of the energy. Error bars represent statistical 1σ errors. Shaded region indicates systematic errors around these center values, defined as the envelope of maximum deviation in $\langle \ln A \rangle$ when using the six perturbations of the baseline simulation. Additional lines show results using alternative values of ϵ with the baseline model.

Fig. 13 compares our results with other published values obtained with Cherenkov telescopes, scintillators, and a variety of coincidence experiments. Our results are consistent with most of the other results that measure cosmic ray composition becoming heavier with energy. These include the air shower experiments KASCADE, MSU and Chacaltaya, the Cherenkov light experiment HE-GRA/AIROBICC, and the air-shower—deep
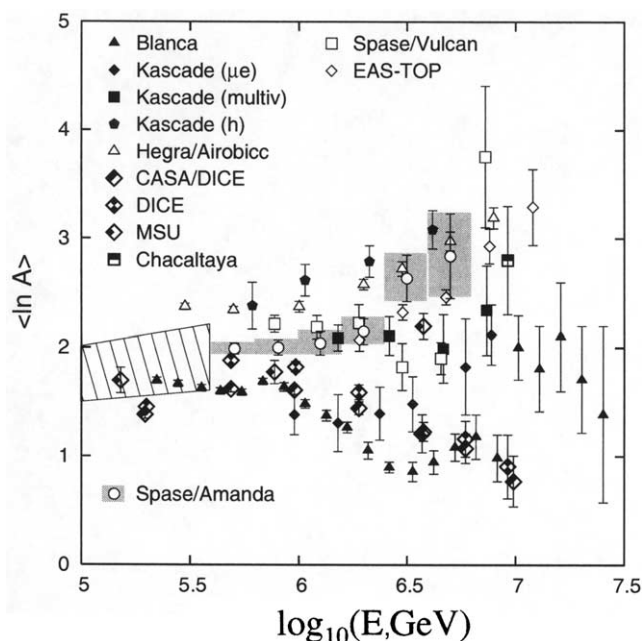
Fig. 13. SPASE/AMANDA composition results compared to other experiments, taken or adapted from [5,10,26–30]. Limits from direct measurements at low energy are shown as lines.

underground muon telescope EAS-TOP/MACRO. SPASE/AMANDA result is in conflict only with the results of BLANCA and DICE (both Cherenkov telescopes) which show the mass becoming lighter in this energy region.

Although each experiment alone has small statistical error bars (as can be seen in Fig. 13), systematic errors are often significant and not displayed in the figure. One can see that many results do not overlap with each other at low energies where there is overlap with direct experiments, suggesting differences in systematic errors between experiments and making them difficult to compare. Systematic errors are a challenge that all experiments have in common, which in many cases dominate the conclusion.

SPASE/AMANDA data indicate an increase of the mass in the energy range from 1 to 6 PeV and improve the current knowledge of the mass composition in the region of the knee. This result is significant because the technique and its sources of systematic error are unique. First, the muon surface energy threshold for detection at depth is about 300 GeV due to the 1500 to 2000 m of solid

ice overburden above the detector. This is high enough for sensitivity to the muons created in the first interactions, yet low enough to overlap with direct measurements for mass composition calibration. Second, the entire high-energy muon bundle is measured over a large volume, and the light output from all muons is sampled over a track length of 500 m and laterally out to 150 m. For a PeV iron primary, AMANDA collects a hundred to several thousand photons over a large volume, allowing a measurement of the total muon bundle energy loss. As a result the combined detectors achieve a mass-independent relative energy resolution of 0.07 in $\log_{10}(E_{prim}/GeV)$. This analysis is also not sensitive to details of the implementation of the photon propagation, because $K50$ measures the light intensity at a constant distance from the muon track. The primary interaction model and the muon propagator are probed only for the difference between proton- and iron-induced showers and their energies. Thus, the method of probing the relative change of muonic (hadronic) energy to electromagnetic energy in the air shower is robust and model independent. The

location of the SPASE site at high altitude is advantageous for the electron component, because the shower maximum is closer to the detector and fluctuations are not as strong as they are at sea level.

However, there is room for improvement. Recent data taken with the larger AMANDA-II array will substantially increase the data statistics. The rate of coincident events between SPASE-2 and AMANDA-II is increased by a factor of 2–3. IceCube [31], the next generation neutrino telescope currently in preparation will include a surface array of one square kilometer in size ($\sim 10^6 \, \mathrm{m \, sr}$). Simulations indicate that both the size and technology will be adequate to measure the mass composition up to 10^{18} eV, well beyond any current result.

References

[1] J.E. Dickinson et al., Nucl. Instrum. Methods A 440 (2000) 95.

[2] J. Ahrens et al., AMANDA Collaboration, Phys. Rev. D 66 (2002) 012005.

[3] K. Greisen, Progr. Cosm. Ray Phys. 3 (1956) 1.

[4] A. Walker et al., Nucl. Instrum Methods A 301 (1991) 574.

[5] J. Hinton, Ph.D. dissertation, University of Leeds, 1998.

[6] J. Ahrens et al., (AMANDA Collaboration), Muon track reconstruction and data selection techniques in AMANDA, Nucl. Instrum. Methods A 524 (2004) 169.

[7] M. Aglietta et al., EAS-TOP and MACRO Collaborations, Phys. Lett. B 337 (1994) 376.

[8] G. Navarra et al., EAS-TOP and LVD Collaborations, Nucl. Phys. B. Proc. Suppl. 70 (1999) 512.

[9] M. Aglietta et al., EAS-TOP and LVD Collaborations, Astropart. Phys. 9 (1998) 185.

[10] M. Aglietta et al., Astropart. Phys. 20 (2004) 641.

[11] T. Gaisser, Cosmic Rays and Particle Physics, Cambridge University Press, 1990.

[12] R.M. Barnett et al., Particle Data Group, Phys. Rev. D 54 (1996) 1.

[13] K. Woschnagg et al., (The AMANDA Collaboration), in: Proceedings of the of the 26th ICRC, Salt Lake City 2, 1999, p. 200.

[14] K. Woschnagg, private communication.

[15] Y.D. He, P.B. Price, J. Geophys. Res. 103 (1998) 17041.

[16] P. Askebjer et al., Appl. Opt. 36 (1997) 4168.

[17] J. Ahrens et al., (AMANDA and SPASE Collaborations), Calibration and survey of AMANDA with the SPASE detectors, Nucl. Instrum. Methods A 522 (2004) 347.

[18] A.M. Hillas, in: Proceedings of the 24th International Cosmic Ray Conference, Rome, vol. 1, 1995, p. 270.

[19] N.N. Kalmykov, S.S. Ostapchenko, Phys. At. Nucl. 56 (3) (1993) 346;
N.N. Kalmykov, S.S. Ostapchenko, A.I. Pavlov, Nucl. Phys. B (Proc. Suppl.) 52B (1997) 17.

[20] P. Lipari, T. Stanev, Phys. Rev. D 44 (1991) 3543.

[21] K. Asakimori (The JACEE Collaboration), in: Proceedings of the 23rd ICRC (Calgary), vol. 2, 1993, p. 21, 25.

[22] A.V. Apanasenko et al., Astropart. Phys. 16 (2001) 13.

[23] P.R. Bevington, D.K. Robinson, Data Reduction and Error Analysis for the Physical Sciences, McGraw-Hill, New York, 1969.

[24] R.S. Fletcher, T.K. Gaisser, P. Lipari, T. Stanev, Phys. Rev. D 50 (1994) 5710;
J. Engel, T.K. Gaisser, P. Lipari, T. Stanev, Phys. Rev. D 46 (1992) 5013.

[25] W. Rhode, D. Chirkin, in: Proc. of the 27th ICRC (Hamburg), 2001, p. HE220.

[26] A. Castellina, Nucl. Phys. Proc. Suppl. 97 (2001) 35.

[27] F. Arqueros et al., A&A 359 (2000) 682.

[28] S.P. Swordy et al., Astropart. Phys. 18 (2002) 129–150, astro-ph/0202159.

[29] K.-H. Kampert, Invited paper at Vulcano Workshop 2002, astro-ph/0212348.

[30] A. Haungs, H. Rebel, M. Roth, Rept. Prog. Phys. 66 (2003) 1145.

[31] J. Ahrens et al., The IceCube Proposal to NSF (2000); J. Ahrens et al., PDD: IceCube Conceptual Design Document (2001). Available from <http://icecube.wisc.edu>.